Shape optimization of fixed-bed reactors in process engineering

Alexis Courtais, Abderrazak Latifi, François Lesage, Yannick Privat

Shape optimization of fixed-bed reactors in process engineering

A. Courtais* A. M. Latifi† F. Lesage‡ Y. Privat§

Abstract

This paper deals with geometric shape optimization of a parallelepipedic fixed-bed reactor with single phase liquid flow where a chemical reaction takes place. The packing is a sort of static mixer made up of solid cylindrical obstacles uniformly distributed in the reactor. The reactive flow is described by means of momentum and mass transport equations in laminar flow regime. The objective is to determine the shape of the packing which maximizes the reaction conversion rate subjected to some specified manufacturing constraints. The optimization approach developed is based on the adjoint system method and the results show that the optimal shape obtained allows to significantly improve the reaction conversion rate. Furthermore, the optimal shape is printed by means of an additive manufacturing technique and several manufacturing constraints mainly related to the thickness of packing are considered.

Keywords: shape optimization, CFD, fixed-bed reactor, additive manufacturing.

AMS classification: 49M05, 65K10, 35Q30.

1 Introduction

Continuous improvement of the competitiveness of the chemical industry requires not only constant innovation, but also an inevitable evolution towards more intensive, efficient, compact and sustainable processes. The shape of the units (reactors, stirrers, packings, exchangers, pipes etc.) that make up the process is one of the key parameters to improve competitiveness and represents a fundamental scientific and technological challenge.
Shape optimization was originally developed in fluid mechanics area, particularly in the design of aircraft wings in aerospace and aeronautics industries. More recently, it has been used in process engineering to determine the optimal shape of a pipe/structure [HP10, DFOP18] or a microchannel [TKH10].
In chemical engineering however where the shape of unit operations is an important design parameter, shape optimization approaches have not been extensively investigated. This important issue deserves therefore to be addressed and will probably result in a paradigm shift in optimal design and operation of processes. Basically, there are three types of shape optimization: parametric, geometric and topologic. In this paper, only geometric optimization is considered, meaning that all

*Laboratoire Réactions et Génie des Procédés, CNRS-ENSIC, Université de Lorraine, Nancy, France. (alexis.courtais@univ-lorraine.fr)
†Laboratoire Réactions et Génie des Procédés, CNRS-ENSIC, Université de Lorraine, Nancy, France. (abderrazak.latifi@univ-lorraine.fr)
‡Laboratoire Réactions et Génie des Procédés, CNRS-ENSIC, Université de Lorraine, Nancy, France. (francois.lesage@univ-lorraine.fr)
§IRMA, Université de Strasbourg, CNRS UMR 7501, 7 rue René Descartes, 67084 Strasbourg, France (yannick.privat@unistra.fr)

admissible designs have the same topology (roughly speaking, the same number of holes). The optimization approach developed is based on the so-called *shape derivative in the sense of Hadamard*, using the adjoint system method. The case study is a 2D fixed-bed reactor with a laminar single phase liquid flow where a homogenous first order chemical reaction takes place. The packing is a kind of static mixer made up of solid cylindrical obstacles uniformly distributed in the reactor. The objective is to determine the shape of the packing which maximizes the reactor conversion rate. Furthermore, when dealing with realistic shapes involved in industrial processes, the obtained optimal shapes must in general meet some manufacturing constraints, which will much depend on the intended application context. Sometimes this is done by post-processing the designed objects. In this paper, a 3D printing technology (i.e. additive manufacturing) is used to manufacture the optimal shape obtained taking into account the specified manufacturing constraints.

The paper is organized as follows: in Section 2, first principles model equations describing the liquid flow in the reactor are introduced. We first investigate an ideal version of the problem where the only manufacturing constraint considered is a volume constraint. We gather the needed material to compute optimal shapes, and introduce in Section 3 an algorithm based on the Hadamard shape derivative combined with an extension-regularization approach of the shape gradient to deal with mesh-displacement. This algorithm is then numerically tested on 2D examples in Section 4. We also propose a more intricate, but also more realistic version of the shape optimization problem, by introducing a constraint on the manufacturing of the optimal shape which will be achieved by means of an additive manufacturing technique. Additive manufacturing (or 3D printing) is opposed to subtractive manufacturing where material is removed to achieve the desired shape. In additive manufacturing, 3D parts are built by adding successive layers of material under computer control. Stratoconception, an additive conception method developed by the CIRTES[1], is particularly well adapted to this use.

2 Modeling and analysis of the shape optimization problem

2.1 Fixed-bed reactor modelling

The fixed-bed reactor considered is a 2D packed bed with a single phase liquid flow where a homogenous first order chemical reaction takes place. The packing is made up of solid cylindrical obstacles (i.e. a kind of static mixer) uniformly distributed in the reactor. Figure 1 shows the schematic representation of the fixed-bed considered.

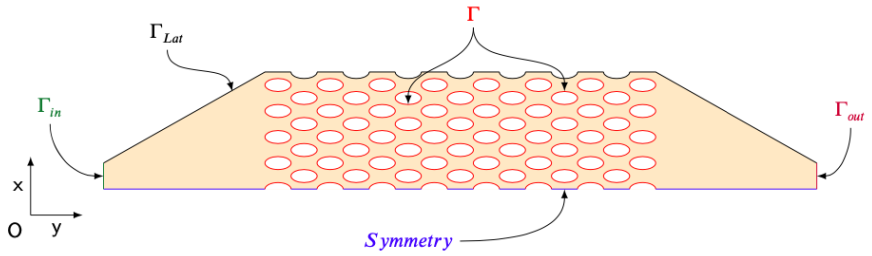

Figure 1: Schematic view of the fixed-bed reactor geometry (that we will use as initialization of the shape optimization algorithm).

[1]namely, the European Center for Rapid Product Development,located in the heart of the Saint-Dié-des-Vosges industrial basin in France.

The optimization method developed in this work is based on the process model equations describing the flow through the fixed-bed reactor. A two-dimensional model is therefore developed in laminar flow regime and involves mass and momentum balance equations. The reactor geometry is modeled by an open bounded domain $\Omega \subset \mathbb{R}^2$, whose boundaries are the union of the inlet Γ_{in}, the outlet Γ_{out}, the lateral wall Γ_{lat} and $\Gamma = \partial\Omega \backslash (\Gamma_{in} \cup \Gamma_{out} \cup \Gamma_{lat})$, the free boundary. Roughly speaking, Γ denotes the boundary of the pores inside the fixed-bed (the regular structure on Fig. 1).

The momentum transport is described by the following Navier-Stokes equations along with the associated boundary conditions:

$$-\nu \Delta \boldsymbol{U} + \boldsymbol{U} \cdot \nabla \boldsymbol{U} + \nabla p = 0 \quad \text{in } \Omega \tag{1a}$$
$$\nabla \cdot \boldsymbol{U} = 0 \quad \text{in } \Omega \tag{1b}$$
$$\boldsymbol{U} = \boldsymbol{U_{in}} \quad \text{on } \Gamma_{in} \tag{1c}$$
$$\boldsymbol{U} = 0 \quad \text{on } \Gamma_{lat} \cup \Gamma \tag{1d}$$
$$\sigma(\boldsymbol{U}, p)\boldsymbol{n} = 0 \quad \text{on } \Gamma_{out} \tag{1e}$$

where $\nu > 0$ denotes the kinematic viscosity of the fluid,

$$\sigma(\boldsymbol{U}, p) = 2\nu\varepsilon(\boldsymbol{U}) - pI \text{ with } \varepsilon(\boldsymbol{U}) = \frac{1}{2}(\nabla \boldsymbol{U} + (\nabla \boldsymbol{U})^\top) \tag{2}$$

is the viscous stress tensor divided by the fluid density, p the fluid kinematic pressure (i.e. the absolute pressure divided by the fluid density), I the identity matrix and $\varepsilon(\boldsymbol{U})$ the strain tensor. The mass balance equations and their associated boundary conditions are given by Eqs. (3) below. It is important to point out that the reaction takes place only in the bulk of the reactor, i.e. in Ω and not on the walls Γ and Γ_{lat}.

$$-D\Delta C + \boldsymbol{U} \cdot \nabla C + kC = 0 \quad \text{in } \Omega \tag{3a}$$
$$C = C_{in} \quad \text{on } \Gamma_{in} \tag{3b}$$
$$\frac{\partial C}{\partial n} = 0 \quad \text{on } \Gamma_{lat} \cup \Gamma_{out} \cup \Gamma \tag{3c}$$

where C denotes the reactant concentration in Ω, $k > 0$ the reaction rate constant and $D > 0$ the constant diffusion coefficient of the reactant.

2.2 Shape optimization problem formulation

Formulating of the shape optimization problem requires the definition of a performance index, decisions variables and constraints, which are introduced below.

Performance index. The objective here is to determine the shape of the fixed-bed reactor (i.e. the position and shape of the free boundary Γ) which maximizes the reaction conversion rate or minimizes the average outlet concentration of the reactant. The performance index is therefore defined by

$$J(\Omega) = \int_{\Gamma_{out}} C \, d\sigma \tag{4}$$

where C denotes the solution of (3).

Decision variable. The decision variable is defined by the free boundary Γ that will evolve with the iterations of the optimization algorithm. The other boundaries are fixed.

Admissible set of constraints. The optimization problem is subjected to different constraints, among which the process model equations (1)-(3). Let Ω_0 be a reference structure for the fixed-bed reactor (typically, the one actually designed in the industry we aim at optimizing). The other constraints consist of :

- an iso-volume constraint introduced in order to guarantee that residence times of admissible shapes have the same order of magnitude. This constraint reads

$$H(\Omega) = 0 \qquad \text{where} \qquad H(\Omega) = |\Omega| - |\Omega_0|, \tag{5}$$

  where $|\Omega|$ denotes as usually the Lebesgue measure of Ω (its surface in 2D).

- an inequality constraint on the energy dissipation by the fluid due to viscous friction and is given by

$$G(\Omega) \leqslant 0 \qquad \text{where} \qquad G(\Omega) = 2\nu \int_\Omega |\varepsilon(\boldsymbol{U})|^2 \, dx - \underbrace{2\nu \int_{\Omega_0} |\varepsilon(\boldsymbol{U})|^2 \, dx}_{\mathcal{E}_0} \leqslant 0. \tag{6}$$

  where $(\boldsymbol{U}, p)$ denotes the solution of (1). Recall that the energy dissipation and the pressure drops are directly correlated. Therefore, such a constraint is necessary since it reflects the fact that the fluid must flow easily through the optimal geometry.

As a conclusion, the first version of the optimal design problem is formulated below. Considering only a geometrical constraint on the volume, and one on the energy dissipated by the fluid leads to the problem:

$$\boxed{\inf_{\Omega \in \mathcal{C}} J(\Omega)} \tag{$\mathcal{P}_1$}$$

where

$$\mathcal{C} := \{\Omega \subset \mathbb{R}^2 \mid \Omega \text{ has a Lipschitz boundary, } H(\Omega) = 0 \text{ and } G(\Omega) \leqslant 0\}. \tag{7}$$

The numerical results for this problem will reveal that pieces of the optimized geometry cannot be easily manufactured by means of the additive manufacturing techniques considered in this work. For this reason, we will propose in Section 4 another version of this optimal design problem where 3D printing constraints are taken into account in order to enable the manufacturing of the computed optimal shape of the reactor.

Remark 1. An important question in the study of such problems is that of the existence of optimal shape(s). Investigating existences issues for general shape optimization problems involving fluid mechanics models is, up to our knowledge, open. Nevertheless, it is likely that imposing additional strong geometrical constraints such as an uniform cone property, will enforce existence (see e.g. [BP13, BOP18, HP10]). Notice also that a similar constraint, unfortunately rather difficult to handle but nevertheless very interesting from the applicative point of view, will also be considered in Section 4.2.

3 Optimization algorithm and numerical results

3.1 Computation of the shape derivative

The numerical resolution of a shape optimization problem of the form ($\mathcal{P}_1$) is based on the knowledge of the derivative of the optimized functional with respect to the variable domain. This notion

can be understood within a variety of frameworks, one of them being the Hadamard boundary variation method which we presently sketch briefly (see e.g. [All07, HP18, MS76, SZ92] for additional explanations).

In the setting of the Hadamard method, variations of a domain Ω with Lipschitz boundary are considered under the form

$$\Omega_{\boldsymbol{\theta}} = (\mathrm{Id} + \boldsymbol{\theta})(\Omega), \tag{8}$$

where $\boldsymbol{\theta} \in W^{1,\infty}(\mathbb{R}^2, \mathbb{R}^2)$ is a 'small' vector field and $\mathrm{Id} : \mathbb{R}^2 \to \mathbb{R}^2$ is the identity mapping.

A shape functional $\Omega \mapsto J(\Omega)$ is said to be shape differentiable at Ω (in the sense of Hadamard) whenever the underlying mapping

$$W^{1,\infty}(\mathbb{R}^2, \mathbb{R}^2) \ni \boldsymbol{\theta} \mapsto J(\Omega_{\boldsymbol{\theta}}) \in \mathbb{R}$$

is Fréchet differentiable at $\boldsymbol{\theta} = 0$. The corresponding derivative $J'(\Omega)(\boldsymbol{\theta})$ is the so-called shape derivative of J at Ω and the following expansion holds:

$$J(\Omega_{\boldsymbol{\theta}}) = J(\Omega) + J'(\Omega)(\boldsymbol{\theta}) + \mathrm{o}(\boldsymbol{\theta}), \qquad \text{where } \frac{\mathrm{o}(\boldsymbol{\theta})}{\|\boldsymbol{\theta}\|_{W^{1,\infty}(\mathbb{R}^2,\mathbb{R}^2)}} \xrightarrow[\boldsymbol{\theta}\to 0]{} 0. \tag{9}$$

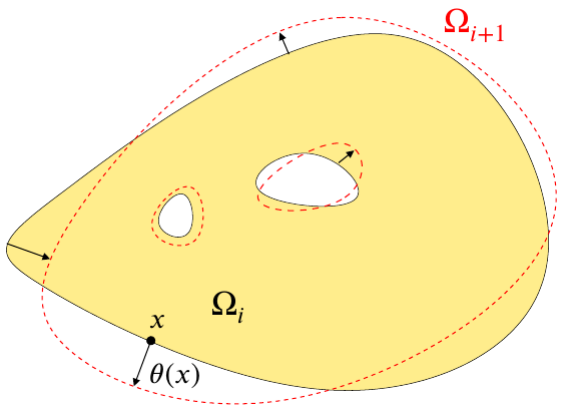

Figure 2: Example of admissible deformation. The domain Ω is plotted with a solid line and $\Omega_{\boldsymbol{\theta}}$ is plotted with a dotted line.

Before computing the shape derivative of J at Ω, let us recall that (1) and (3) have to be understood through their variational form. Let Ω denote a given element of $\mathcal{C}$. We introduce the functional spaces

$$\begin{aligned}
\mathcal{U} &= \{(\boldsymbol{U}, p) \in H^1(\Omega, \mathbb{R}^2) \times L^2(\Omega, \mathbb{R}) \mid \operatorname{div} \boldsymbol{U} = 0 \text{ in } \Omega \text{ and } \boldsymbol{U} = \boldsymbol{U}_0 \text{ on } \Gamma_{in}\} \\
\mathcal{V} &= \{(\boldsymbol{w}, q) \in H^1(\Omega, \mathbb{R}^2) \times L^2(\Omega, \mathbb{R}) \mid \operatorname{div} \boldsymbol{w} = 0 \text{ in } \Omega \text{ and } \boldsymbol{w} = 0 \text{ on } \Gamma_{in}\} \\
\mathcal{W} &= \{C \in H^1(\Omega, \mathbb{R}) \mid C = C_0 \text{ on } \Gamma_{in}\} \\
\mathcal{X} &= \{u \in H^1(\Omega, \mathbb{R}) \mid u = 0 \text{ on } \Gamma_{in}\}
\end{aligned}$$

The variational formulation associated to (1) reads: find $(\boldsymbol{U}, p) \in \mathcal{U}$ such that

$$\forall (\boldsymbol{w}, q) \in \mathcal{V}, \qquad \int_\Omega \varepsilon(\boldsymbol{U}) : \varepsilon(\boldsymbol{w}) + (\boldsymbol{U} \cdot \nabla \boldsymbol{U})\boldsymbol{w} - q \operatorname{div} \boldsymbol{U} = 0$$

and the variational formulation associated to (3) reads: find $C \in \mathcal{W}$ such that

$$\forall u \in \mathcal{X}, \qquad \int_\Omega (D\nabla C \cdot \nabla u + (\boldsymbol{U} \cdot \nabla C)u + kCu) = 0$$

The following well-posed results for the solutions of the PDEs (1) and (3) is rather standard. We refer for instance to [BF13, Tem84] for the fluid system and to [Boy05] for the convection-diffiusion equation. A very close system is also investigated in [FAB+19]. The following theorem sums-up the well-posed character of the coupled system (1)-(3).

Theorem 1. *Let $\boldsymbol{U}_0 \in H^{1/2}(\Gamma_{in}, I\!R^2)$ and $C_0 \in H^{1/2}(\Gamma_{in}, I\!R)$. If the viscosity ν is assumed to be large enough, then System (1)-(3) has a unique solution $(\boldsymbol{U}, p)$ in $\mathcal{U}$. Similarly, the problem (3) has a unique solution C in $\mathcal{W}$.*

Let us now compute the shape derivative of J. The shape differentiability of J is a standard issue, which is well referenced in the dedicated literature and has been much studied. Regarding the case we investigate, we claim that a standard approach, as described in [HP18, Chap. 5] would allow us to answer positively to this issue. The key point is to start from the variational formulation associated to the PDE problem on the deformed domain $\Omega_{\boldsymbol{\theta}}$, to use a change of variable to rewrite all the involved integrals on a fixed domain, and finally to use adequately the implicit function theorem to get the shape differentiability of the solutions of the PDEs under consideration. Very close differentiability studies have been led in [FAB+19, BOP18]. Let us first formally introduce the tools for computing the shape derivatives.

Let $\Omega \in \mathcal{C}$ and $\boldsymbol{\theta} \in W^{1,\infty}(\mathbb{R}^2, \mathbb{R}^2)$ be a vector field whose support does not intersect Γ_{in}, Γ_{lat} and Γ_{out}. Let us compute $J'(\Omega)(\boldsymbol{\theta})$ defined by (9). By following [All07, HP18, DFOP18]), one gets

$$J'(\Omega)(\boldsymbol{\theta}) = \frac{d}{dt}\int_{\Gamma_{out}} C_t \, d\sigma\Big|_{t=0} = \int_{\Gamma_{out}} C' \, d\sigma \tag{10}$$

where C_t denotes the solution of (3) on the domain $(\mathrm{Id} + t\boldsymbol{\theta})(\Omega)$, $\boldsymbol{U'}$, p' and C' denote respectively the so-called Eulerian derivatives of $\boldsymbol{U}$, p and C. From a qualitative point of view, $\boldsymbol{U'}$ (resp. p' and C') stands for the sensitivity of $\boldsymbol{U}$ (resp. p and C) with respect to shape variations. Standard differentiation formula (see [MP10, dLSMP11, HP10]) enable us to show that $(\boldsymbol{U'}, p') \in \mathcal{V}$ solves (in a variational sense) the system

$$-\nu\Delta\boldsymbol{U}' + (\boldsymbol{U'} \cdot \nabla)\boldsymbol{U} + (\boldsymbol{U} \cdot \nabla)\boldsymbol{U'} + \nabla p' = 0 \quad \text{in } \Omega \tag{11a}$$

$$\nabla \cdot \boldsymbol{U'} = 0 \quad \text{in } \Omega \tag{11b}$$

$$\boldsymbol{U'} = 0 \quad \text{on } \Gamma_{in} \cup \Gamma_{lat} \tag{11c}$$

$$\boldsymbol{U'} = -\frac{\partial \boldsymbol{U}}{\partial n}(\boldsymbol{\theta} \cdot \boldsymbol{n}) \quad \text{on } \Gamma \tag{11d}$$

$$\sigma(\boldsymbol{U'}, p')\boldsymbol{n} = 0 \quad \text{on } \Gamma_{out} \tag{11e}$$

Similarly, C' stands for the sensitivity of C with respect to shape variations of Ω and C' solves in a variational sense the system.

$$-D\Delta C' + \boldsymbol{U} \cdot \nabla C' + \boldsymbol{U'} \cdot \nabla C + kC' = 0 \quad \text{in } \Omega \tag{12a}$$

$$C' = 0 \quad \text{on } \Gamma_{in} \tag{12b}$$

$$\frac{\partial C'}{\partial n} = -\frac{\partial^2 C}{\partial n^2}(\boldsymbol{\theta} \cdot \boldsymbol{n}) + \nabla C \cdot (\nabla(\boldsymbol{\theta} \cdot \boldsymbol{n}) - (\nabla(\boldsymbol{\theta} \cdot \boldsymbol{n}) \cdot \boldsymbol{n})\boldsymbol{n}) \quad \text{on } \Gamma \tag{12c}$$

$$\frac{\partial C'}{\partial n} = 0 \quad \text{on } \Gamma_{out} \cup \Gamma_{lat} \tag{12d}$$

Unfortunately, the formula (10) of the shape derivative is not very exploitable as it is. To overcome this problem, it is relevant to rewrite it as an integral on the free boundary. For this purpose, let us introduce the adjoint variables C_a as the solution of the diffusion system

$$
\begin{aligned}
-D\Delta C_a - \boldsymbol{U}\cdot\nabla C_a + kC_a &= 0 \quad && \text{in } \Omega && \text{(13a)}\\
C_a &= 0 \quad && \text{on } \Gamma_{in} && \text{(13b)}\\
\frac{\partial C_a}{\partial n} &= 0 \quad && \text{on } \Gamma_{lat}\cup\Gamma && \text{(13c)}\\
C_a(\boldsymbol{U}\cdot\boldsymbol{n}) + D\frac{\partial C_a}{\partial n} &= 1 \quad && \text{on } \Gamma_{out} && \text{(13d)}
\end{aligned}
$$

and the variables $(\boldsymbol{U}_a, p_a)$ as the solution of the linearized Navier-Stokes system

$$
\begin{aligned}
-\nu\Delta\boldsymbol{U_a} + (\nabla\boldsymbol{U})^\top\boldsymbol{U_a} - \nabla\boldsymbol{U_a}\boldsymbol{U} + \nabla p_a &= -C_a\nabla C \quad && \text{in } \Omega && \text{(14a)}\\
\nabla\cdot\boldsymbol{U_a} &= 0 \quad && \text{in } \Omega && \text{(14b)}\\
\boldsymbol{U_a} &= 0 \quad && \text{on } \Gamma_{in}\cup\Gamma_{lat}\cup\Gamma && \text{(14c)}\\
\sigma(\boldsymbol{U_a}, p_a)\boldsymbol{n} + (\boldsymbol{U}\cdot\boldsymbol{n})\boldsymbol{U_a} &= 0 \quad && \text{on } \Gamma_{out} && \text{(14d)}
\end{aligned}
$$

where $(\boldsymbol{U}, p, C)$ denotes the solution of the coupled system (1)-(3)

A workable writing of the shape derivative $J'(\Omega)(\boldsymbol{\theta})$ is thus derived in the following result.

Theorem 2. *Let $\boldsymbol{U}_0 \in H^{1/2}(\Gamma_{in}, I\!R^2)$ and $C_0 \in H^{1/2}(\Gamma_{in}, I\!R)$. If the viscosity ν is assumed to be large enough, System (13)-(14) has a unique solution $(C_a, \boldsymbol{U}_a, p_a)$ in $\mathcal{X}\times\mathcal{V}$.*

Furthermore, let $\boldsymbol{\theta} \in W^{1,\infty}(I\!R^2, I\!R^2)$ be a vector field whose support does not intersect Γ_{in}, Γ_{lat} and Γ_{out}. If one assumes that the state and adjoint variables $\boldsymbol{U}$, $\boldsymbol{U}_a$, C and C_a have H^2 regularity in their domain of definition, then there holds

$$
J'(\Omega)(\boldsymbol{\theta}) = \int_\Gamma \left(2\nu\varepsilon(\boldsymbol{U}) : \varepsilon(\boldsymbol{U_a}) - DC_a\Delta C\right)(\boldsymbol{\theta}\cdot\boldsymbol{n})\, d\sigma.
$$

A proof of this result is provided in Appendix A.

3.2 A Lagrangian approach

The shape optimization approach developed hereafter is a gradient-based method which uses the so-called Hadamard boundary variation method [HP18] described in Section 3.1. To take the constraints into account in Problem ($\mathcal{P}_1$), it is convenient to introduce the Lagrangian functional associated to the optimization problem, namely the functional $\mathcal{L}$ given by

$$
\mathcal{L}(\Omega, \lambda_{\mathcal{V}}, \lambda_{\mathcal{E}}) = K_{crit}J(\Omega) + \lambda_{\mathcal{V}}H(\Omega) + \lambda_{\mathcal{E}}G(\Omega), \tag{15}
$$

where $K_{crit} > 0$ denotes a constant allowing to homogenize the Lagrangian functional. $\lambda_{\mathcal{V}} \in \mathbb{R}$ and $\lambda_{\mathcal{E}} \in \mathbb{R}_+$ stand for the Lagrange multipliers respectively associated to the constraints $H(\Omega) = 0$ and $G(\Omega) \leqslant 0$.

Before providing the main idea of the algorithm, we need to compute the shape derivative of $\mathcal{L}$. Let $\boldsymbol{\theta} \in W^{1,\infty}(\mathbb{R}^2, \mathbb{R}^2)$ be a vector field whose support does not intersect Γ_{in}, Γ_{lat} and Γ_{out}. We denote by $\mathcal{L}'(\Omega, \lambda_{\mathcal{V}}, \lambda_{\mathcal{E}})(\boldsymbol{\theta})$ the shape derivative of $\mathcal{L}$ (with respect to its first variable), in other words

$$
\mathcal{L}'(\Omega, \lambda_{\mathcal{V}}, \lambda_{\mathcal{E}})(\boldsymbol{\theta}) = \lim_{t\searrow 0}\frac{\mathcal{L}(\Omega_t) - \mathcal{L}(\Omega)}{t}, \qquad \text{with} \qquad \Omega_t = (\mathrm{Id} + t\boldsymbol{\theta})(\Omega).
$$

Let us introduce the adjoint state $(\boldsymbol{U_a}, p_a)$ as the solution of the system

$$\mathcal{L}(\boldsymbol{U_a}, \nabla p_a) = -\lambda_{\mathcal{E}} 2\nu\Delta\boldsymbol{U} - K_{crit}C_a\nabla C \quad \text{in } \Omega \tag{16a}$$
$$\nabla \cdot \boldsymbol{U_a} = 0 \quad \text{in } \Omega \tag{16b}$$
$$\boldsymbol{U_a} = 0 \quad \text{on } \Gamma_{in} \cup \Gamma_{lat} \cup \Gamma \tag{16c}$$
$$\sigma(\boldsymbol{U_a}, p_a)\boldsymbol{n} + (\boldsymbol{U}\cdot\boldsymbol{n})\boldsymbol{U_a} = 4\nu\lambda_{\mathcal{E}}\varepsilon(\boldsymbol{U})\boldsymbol{n} \quad \text{on } \Gamma_{out} \tag{16d}$$

where $\mathcal{L}(\boldsymbol{U_a}, \nabla p_a) = -\nu\Delta\boldsymbol{U_a} + (\nabla\boldsymbol{U})^\top\boldsymbol{U_a} - \nabla\boldsymbol{U_a}\boldsymbol{U} + \nabla p_a$ and C_a as the solution of the system

$$-D\Delta C_a - \boldsymbol{U}\cdot\nabla C_a + kC_a = 0 \quad \text{in } \Omega \tag{17a}$$
$$C_a = 0 \quad \text{on } \Gamma_{in} \tag{17b}$$
$$\frac{\partial C_a}{\partial n} = 0 \quad \text{on } \Gamma_{lat} \cup \Gamma \tag{17c}$$
$$C_a(\boldsymbol{U}\cdot\boldsymbol{n}) + \mathcal{D}\frac{\partial C_a}{\partial n} = 1 \quad \text{on } \Gamma_{out} \tag{17d}$$

Proposition 1. *Under the same assumptions as in Theorem 2, the coupled system (17)-(16) has a unique solution $(C_a, \boldsymbol{U}_a, p_a)$ in $\mathcal{X}\times\mathcal{V}$ and there holds*

$$\mathcal{L}'(\Omega, \lambda_{\mathcal{V}}, \lambda_{\mathcal{E}})(\boldsymbol{\theta}) = \int_\Omega \left(2\nu(\varepsilon(\boldsymbol{U}) : \varepsilon(\boldsymbol{U_a}) - \lambda_{\mathcal{E}}\varepsilon(\boldsymbol{U}) : \varepsilon(\boldsymbol{U})) - K_{crit}DC_a\Delta C + \lambda_{\mathcal{V}}\right)(\boldsymbol{\theta}\cdot\boldsymbol{n})\, d\sigma.$$

It is notable that the shape gradient $g(\Omega)$, defined on the free boundary Γ, is therefore given by

$$g(\Omega) = 2\nu(\varepsilon(\boldsymbol{U}) : \varepsilon(\boldsymbol{U_a}) - \lambda_{\mathcal{E}}\varepsilon(\boldsymbol{U}) : \varepsilon(\boldsymbol{U})) - K_{crit}DC_a\Delta C + \lambda_{\mathcal{V}}. \tag{18}$$

Its computation needs the knowledge of all the state and adjoint variables ($\boldsymbol{U}$, p and C) and ($\boldsymbol{U}_a$, p_a and C_a). From the numerical point of view, we will use the gradient to build an iterative optimization algorithm. In a nutshell, at each iteration, we will infer a displacement vector field $\boldsymbol{\theta}$ (a descent direction of the Lagrangian) from the knowledge of $g(\Omega)$ and modify adequately each node of the mesh.

Let us explain how to compute the vector field $\boldsymbol{\theta_i}$ At the iteration i ($i \in \mathbb{N}^*$). Consider the domain Ω_i obtained after i iterations of the algorithm. The vector field $\boldsymbol{\theta_i}$ is determined in such a way that

$$\mathcal{L}'(\Omega, \lambda_{\mathcal{V}}, \lambda_{\mathcal{E}})(\boldsymbol{\theta_i}) = -\gamma\|\nabla\boldsymbol{\theta_i}\|^2_{L^2(\Omega_i)} - \|\boldsymbol{\theta_i}\|^2_{L^2(\Omega_i)}.$$

Observe that $\gamma\|\nabla\cdot\|^2_{L^2(\Omega_i)} + \|\cdot\|^2_{L^2(\Omega_i)}$ defines a norm equivalent to the standard H^1 norm. The introduction of the parameter γ will allow us to adjust the diffusivity strength on the mesh.

The choice of this modified H^1 norm is motivated by the willing of getting a smooth enough vector field. Such an issue has been much discussed in [DMNV07] and yields to defining $\boldsymbol{\theta_i}$ as the unique solution (in a weak variational sense) of the PDE

$$-\gamma\Delta\boldsymbol{\theta} + \boldsymbol{\theta} = 0 \quad \text{in } \Omega \tag{19a}$$
$$\boldsymbol{\theta} = 0 \quad \text{on } \Gamma_{in} \cup \Gamma_{out} \cup \Gamma_{Lat} \tag{19b}$$
$$\gamma\nabla\boldsymbol{\theta}\boldsymbol{n} = -g\boldsymbol{n} \quad \text{on } \Gamma \tag{19c}$$

Once the vector field $\boldsymbol{\theta}$ computed, we then move all mesh-nodes according to

$$\Omega_{i+1} = (\mathrm{Id} + t_i\boldsymbol{\theta_i})(\Omega_i)$$

where $t_i > 0$ is the method step which must be chosen adequately (for instance with the help of a 1D optimization method), Id is the identity operator.

3.3 Optimization algorithm

The numerical optimization problem presented in this work is implemented within OpenFOAM environment which is a free and open source software [WTJF98]. This CFD software solves numerically a large range of PDEs using the Finite Volume Method. In our case, OpenFOAM solves the system of Navier-Stokes equations (1) combined with the mass balance equations (3), the adjoint system equations (13)-(14)) and computes the mesh diffusion displacement through (19). The Python library named ''*pyFoam* '' is used in order to connect optimization iterations to each other using its utility ''*pyFoamMeshUtilityRunner.py* ''. The developed algorithm consists of the folowing steps:

1. Meshing of the initial shape using `cfMesh` and `snappyHexMesh`, two mesh utilities supplied by OpenFOAM.
   According to (18), the shape gradient functional is defined on the free boundary and depends on the first and second order derivatives of the state and adjoint variables. Therefore, all these quantities need to be computed with accuracy near wall zones, and we therefore add 2 layers of mesh near the boundary Γ.

2. Resolution of the process model equations (1)-(3) and the adjoint system equations (13)-(14). The SIMPLE algorithm is used in order to deal with the velocity-pressure coupling of Eqs. (1)-(14).

3. The shape gradient $g(\Omega)$ and the mesh diffusion $\boldsymbol{\theta}$ are computed. The obstacle and channel constraints are taken into account during this step (see § 4.2).

4. Update of the Lagrange multipliers at the k-th iteration according to the following relations:

$$\lambda_{\mathcal{V}}^{k+1} = \lambda_{\mathcal{V}}^{k} + \beta_{\mathcal{V}} H(\Omega) \tag{20}$$

$$\lambda_{\mathcal{E}}^{k+1} = \max\left(0, \lambda_{\mathcal{E}}^{k} + \beta_{\mathcal{E}} G(\Omega)\right) \tag{21}$$

   In these equations, $\beta_{\mathcal{V}}$ and $\beta_{\mathcal{E}}$ denote small positive parameters.

5. At the end of iterations, a mesh quality test using three criteria is performed and a test on the convergence is carried out. Fig. 3 illustrates the mesh quality criteria. According to [Hol15], the criteria are:

   - the **mesh aspect ratio** defined as the ratio of the longest side over the shortest one among all cells of the mesh, namely $r = l/s$ on Fig. 3.
   - the **mesh non-orthogonality** which corresponds to the angle between the line linking two adjacent cell centers and the normal to their common face, namely the angle $\alpha = \arccos(\frac{A_i \cdot C_i}{|A_i||C_i|})$ on Fig. 3.
   - the **face skewness** which is the ratio of the distance $|d_i|$ over the distance $|C_i|$, where $|d_i|$ denotes the distance between the intersection of the line linking two adjacent cell centers with their common face and their common face center, and $|C_i|$ denotes the distance between the two considered cell centers.

   The remeshing process takes place whenever the aforementioned criteria are greater than 10, 65 and 3.8 respectively. The convergence criterion of the algorithm is the ratio of the standard deviation of the 50 last Lagrangian values over the average of these 50 values. If the ratio is less than 10^{-4}, the algorithm stops.

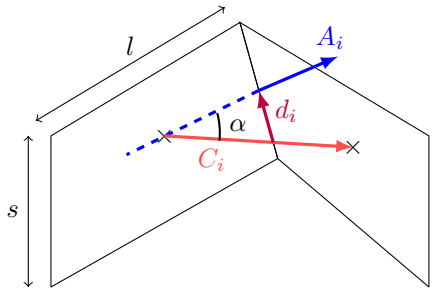

Figure 3: Illustration of the mesh quality criteria.

4 Numerical results and discussion

This section is devoted to the presentation of the numerical results obtained by implementing the algorithm described in Section 3.3. We also enrich our model by introducing a modified version of the shape optimization problem ($\mathcal{P}_1$), taking into account several manufacturing constraints. In the following sections, we introduce the new criteria we will deal with, as well as a simple optimization algorithm. We obtain promising results, and we are working at this time on improvements of the manufacturing constraints treatment.

4.1 Numerical solution of Problem ($\mathcal{P}_1$)

Figure 4 illustrates the concentration profiles of the reactant for : (a) the initial design of the reactor, (b) optimal shapes for Problem ($\mathcal{P}_1$), by following to the algorithm described in Section 3.3.

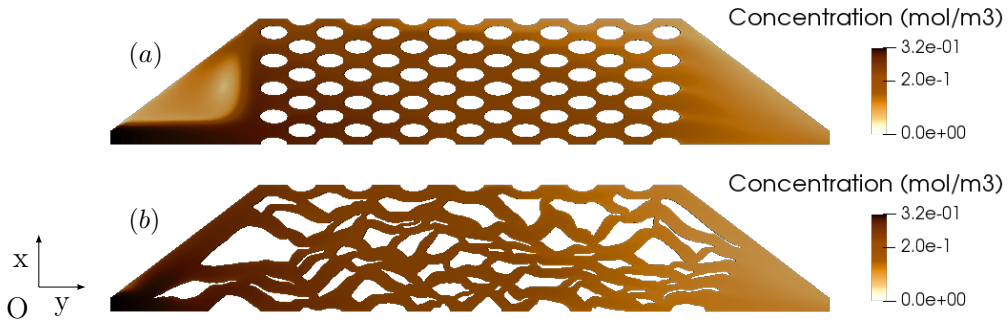

Figure 4: Initial configuration of the fixed-bed reactor (a), optimized shape without manufacturing constraint (b).

As we can see, a dead zone arises at the reactor inlet of the initial configuration. This dead zone is a region where the reactant concentration is low which produces a low reaction rate (recall that the conversion rate is proportional to the reactant concentration $r = kC$). As a result, this reactor dead volume is almost useless.

As an illustration of the method efficiency, we provide on Fig. 5 the convergence curves related to this shape optimization problem, namely the evolution of the Lagrangian functional, the performance index and the two constraints H and G with respect to the iteration number. According

to Fig. 5, the performance index has decreased by almost 10 % which will improve the conversion rate accordingly. The volume and energy dissipation constraints are satisfied and it is interesting to point out that the energy inequality constraint is active.

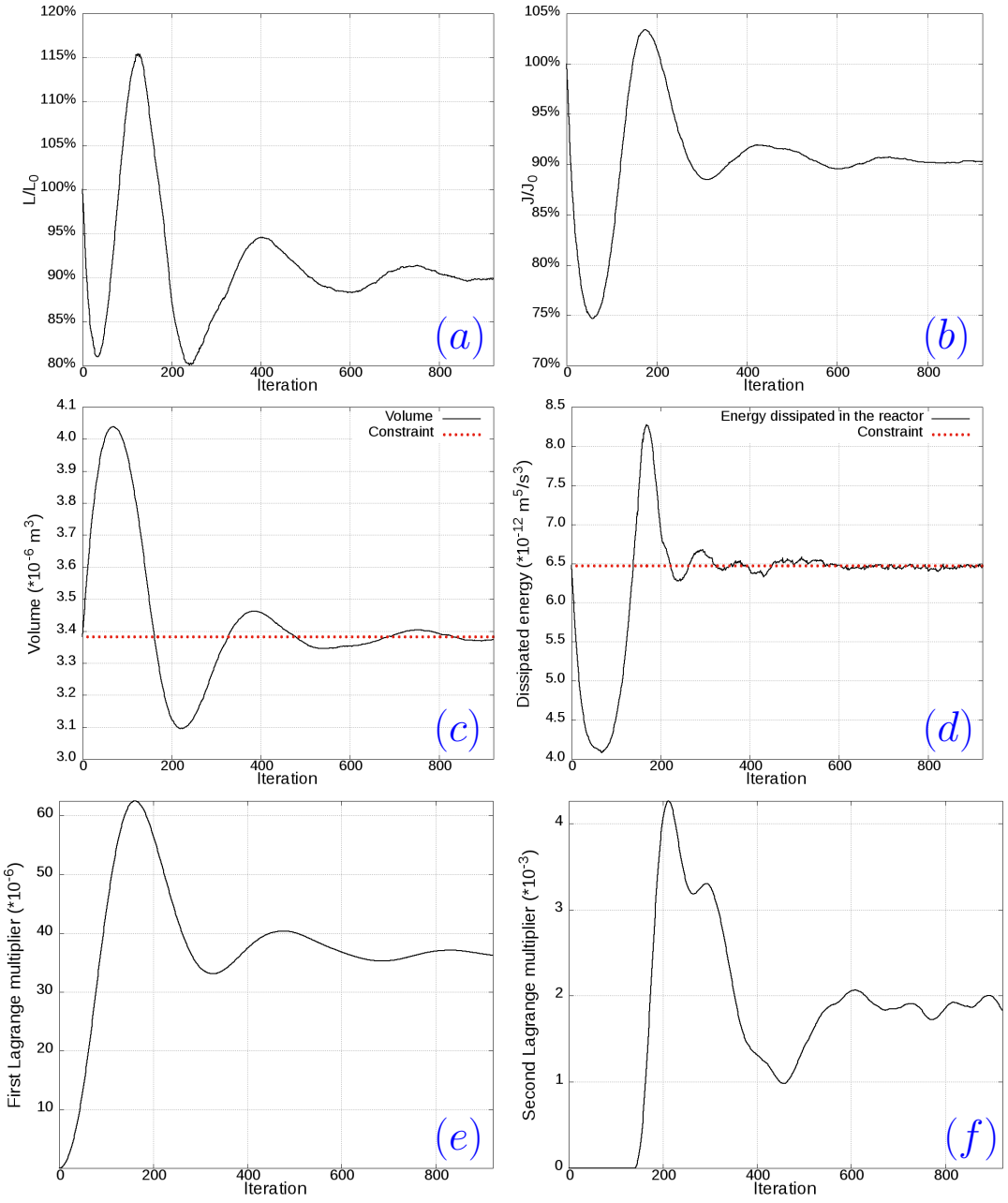

Figure 5: Convergence curves of the optimization process, (a) is the ratio $\frac{\mathcal{L}}{\mathcal{L}_0}$, (b) the ratio $\frac{J}{J_0}$, (c) the volume constraint, (d) the energy disspation constraint, (e) the Lagrange multiplier associated to the volume constraint and (f) the Lagrange multiplier associated to the energy constraint over iterations.

However, these first results are unfortunately not directly usable for practical purposes if fixed-bed reactors are to be built by means of an additive manufacturing technique. Indeed, the stratoconception process used to build the reactor requires minimal width on channels and obstacles making the process and the designed object robust. In the following sections, we slightly modify our approach to take into account the manufacturing constraints.

4.2 New version of the optimization problem: introduction of manufacturing constraints

Since the resulting optimal shape will be manufactured by means of a 3D printing technique, additional constraints should be accounted for in the optimization problem. The new optimization problem is obtained by adding these new constraints on the formulation ($\mathcal{P}_1$).

They are of inequality type and impose minimum values on the pores width (domain Ω) and on the packing "thickness". There are several ways of modeling such a constraint. Let us describe hereafter the chosen approach.

It is not straightforward to define and use minimum thickness constraints inside a Lagrangian functional. The manufacturing constraints taken into account during the mesh diffusion step modify the vector field $\boldsymbol{\theta}$ after computation. This approach corresponds to a projected gradient type method. The obstacle and channel constraints are not considered using the same algorithm. Let us provide hereafter some explanations about these facts.

The method considered in the present paper aims to improve an existing design to include the manufacturing constraints. Since the objective of this work is not centered on manufacturability issues, we propose in the following a rather naive approach to take into account manufacturing constraints in order to quickly obtain first results. We are currently working on improving the consideration of such constraints, by drawing inspiration from the much more advanced works [AJM16, ADFM17, ADE+17a, ADE+17b] on the subject, which cleverly includes these constraints within an algorithm using a dual version of the optimization problem.

4.2.1 Obstacle minimum thickness constraint

The approach we chose is based on the notion of *reach* of a set [Fed59]. Let $h > 0$. A closed set A is said to have a reach larger than h provided that every point x belonging to $\{x \in \mathbb{R}^2 \mid \text{dist}(x, A) < h\}$ has a unique projection point on A. The supremum of such h is called the reach of A, and denoted as $\text{reach}(A)$. We will impose a thickness constraint by imposing the constraint

$$T(\Omega) \geqslant 0 \qquad \text{where} \qquad T(\Omega) = \text{reach}({}^{c}\Omega) - d_{\min}^{\text{obstacle}},$$

where $d_{\min}^{\text{obstacle}} > 0$ denotes the minimal obstacle width constraint and ${}^{c}\Omega$ the complement set of Ω in the domain delimited by Γ_{in}, Γ_{out} and Γ_{lat} (i.e. the full domain without pores).

This obstacle constraint is taken into account in 2 main steps: the first one involves the construction of the skeleton of each obstacle defined as follows: for each obstacle, the skeleton is the set of points such that their distance to the boundary of the obstacle is achieved for at least two distinct points of the boundary.

The algorithm allowing us to construct the skeleton reads as follows:

1. The Voronoi diagram of the boundary points is computed. This diagram of a set of points E is constructed from the Voronoi regions. In two-dimension, the Voronoi region of a point x is defined as the area where points belonging to the area is closest to point x than all other points of E [Att95] (see Fig 6 for an illusatration). The mathematical definition is given in Definition 1 below.

Definition 1. *Let X a subset of $\mathbb{R}^d$ and $P = \{P_1, P_2, ..., P_n\} \subset X$ a set of points. The Voronoi region R_k of the point P_k is defined as*

$$R_k = \{x \in X \,|\, d(x, P_k) < d(x, P_j), \quad \forall j \neq k\}$$

where $d(x, P_k)$ denotes the distance between x and P_k.

Each edge of the Voronoi diagram is the boundary of 2 Voronoi regions and the intersections of edges, called vertices of the diagram, are the boundary of 3 (or more) Voronoi regions. Each edge is bounded by 2 vertices. The skeleton is constructed from the edges of the Voronoi diagram.

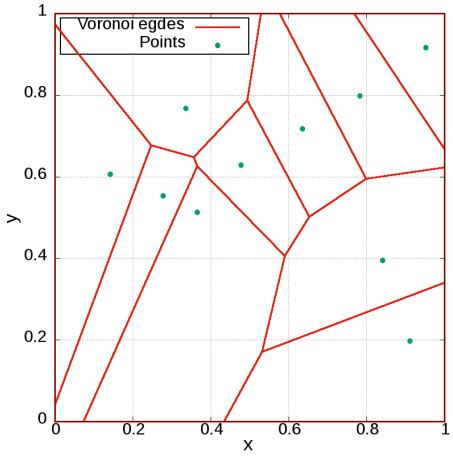

Figure 6: Voronoi diagram of a 10-point set.

2. The Voronoi diagram (Fig. 7(a)) is then simplified into two steps in order to compute the skeleton Sk.

   - Only edges completely included in the skeleton are kept (Fig. 7(b)).
   - A second simplification is carried our by means of 2 criteria. (i) For all Voronoi vertices s, the first criterion is the function $r(s)$ that associates the maximum disc radius centered in s. (ii) Each point s has three (or more) projections on the skeleton, called p_1, p_2 and p_3, the second criterion is given by $\alpha(s) = \max(\widehat{p_1 s p_2}, \widehat{p_1 s p_3}, \widehat{p_2 s p_3})$. The lower bound of those criteria is respectively 2.10^{-4} m and $\frac{\pi}{4}$ (Fig. 7(c)).

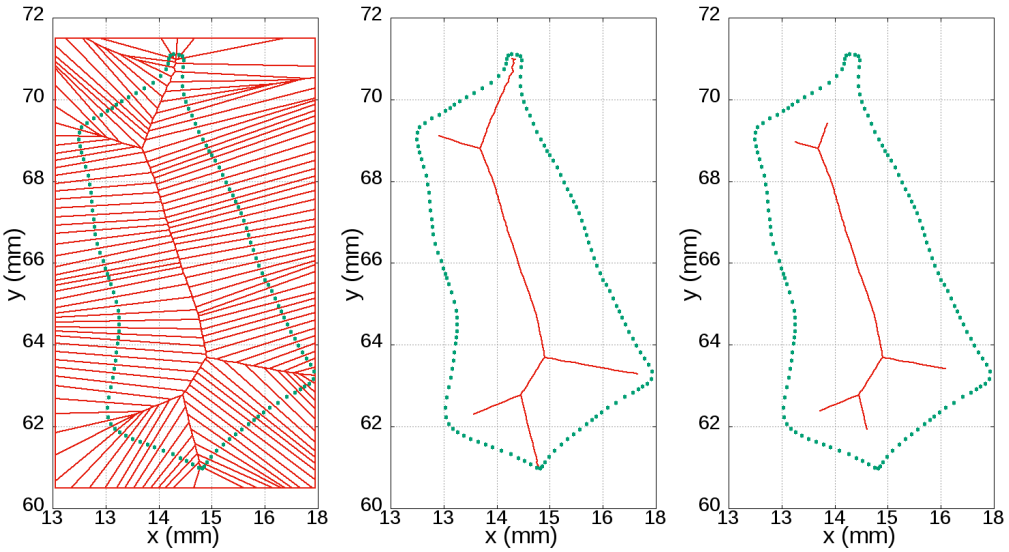

(a) Obstacle Voronoi diagram (b) First simplification (c) Second simplification: skeleton

Figure 7: Simplification of the Voronoi diagram into the skeleton, green points denote obstacle points and red line denotes Voronoi diagram (a) and the simplified skeleton (b) and (c).

Once the skeleton constructed, a test on the minimum distance between the obstacle and the skeleton named $d(x)$ is performed. If this distance $d(x)$ is lower than $d_{\min}^{\text{obstacle}}/2$ and $d(x) > d\big(x + t\boldsymbol{\theta}(x)\big)$ then the vector $\boldsymbol{\theta}(x)$ is projected to the corresponding skeleton tangent vector.

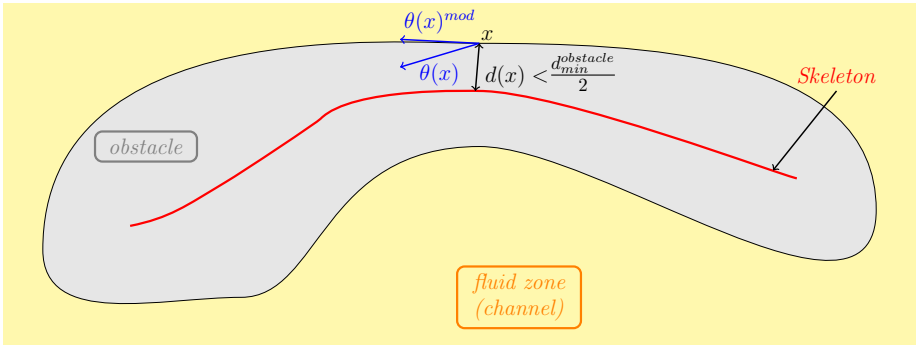

Figure 8: Illustration of the obstacle constraint consideration.

4.2.2 Channel minimum width constraint

The channel constraints are taken into account as follows (see the illustration on Fig. 9):

1. For each boundary point x of a given obstacle, determine the nearest boundary point x^{near} belonging to another obstacle boundary.
2. We compute the inner product $\boldsymbol{xx^{near}} \cdot \boldsymbol{\theta}(x)$. If $\boldsymbol{xx^{near}} \cdot \boldsymbol{\theta}(x) > 0$ and $\|\boldsymbol{xx^{near}}\| < d_{\min}^{\text{channel}}$ then the vector $\boldsymbol{\theta}(x)$ is projected on the orthogonal line to the vector $\boldsymbol{xx^{near}}$.

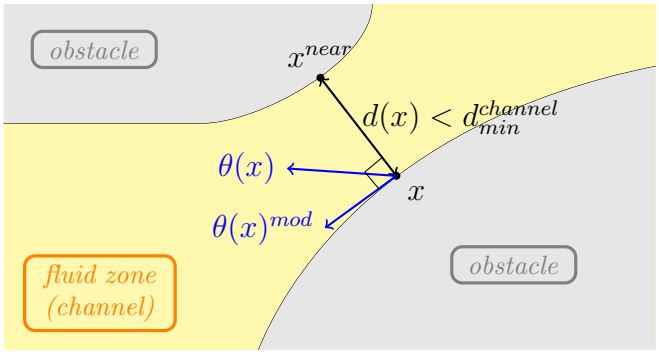

Figure 9: Illustration of the channel constraint treatment.

4.3 Fixed-bed reactor optimization under energy, volume and manufacturing constraints

We investigate hereafter how is the optimal design modified whenever manufacturing constraints are added to the optimization algorithm in order to design the optimal reactor. The lower bounds of the obstacle thickness and the channel width imposed by the manufacturing process are respectively $2\,10^{-3}$ m and $2.1\,10^{-3}$ m. On Figure 10, we provide a comparison of the concentration profiles of the reactant for : (a) the optimal shape obtained for Problem ($\mathcal{P}_1$) (without manufacturing constraints) and (b) optimal shapes when width constraints are integrated to the algorithm. Similarly to what was observed in the case (a), no dead zone arises when taking into account the manufacturing constraints, even if stratoconception process used to build the reactor requires minimal width on channels and obstacles. Figure 11 presents a virtual image of the optimal reactor (b) manufactured by stratoconception process. On both configurations, we can see that the dead zone vanished which will improve the performances of the reactor.

The residence time distributions (RTD) of the initial and optimized designs under manufacturing constraints are presented on Fig. 12. In chemical engineering, the RTD is defined as the statistical time distribution that a set of particles stays in the reactor. It allows to characterize the reactor hydrodynamics. The RTD curves show a better homogeneity of the fluid flow in the optimized configuration (Fig. 10(b)) where the standard deviation is 3.5 times lower than in the initial configuration (21 vs 73s). This better homogeneity can also be observed on Fig. 12 where the concentration gradient in the horizontal direction is much larger in the initial shape than in the optimized one. Finally, the disappearance of the dead region along with the better homogeneity of the flow improve the performance index by 10%.

5 Conclusion and perspectives

In this paper, we have developed a geometric shape optimization approach for the design and sizing of processes. We are more specifically interested in the shape of the packing of a fixed-bed reactor with a single-phase liquid flow involving a chemical reaction in laminar flow regime. Furthermore, the packing configuration which minimizes the average concentration of the reagent at the outlet of the reactor while satisfying the process model equations and the volume, the

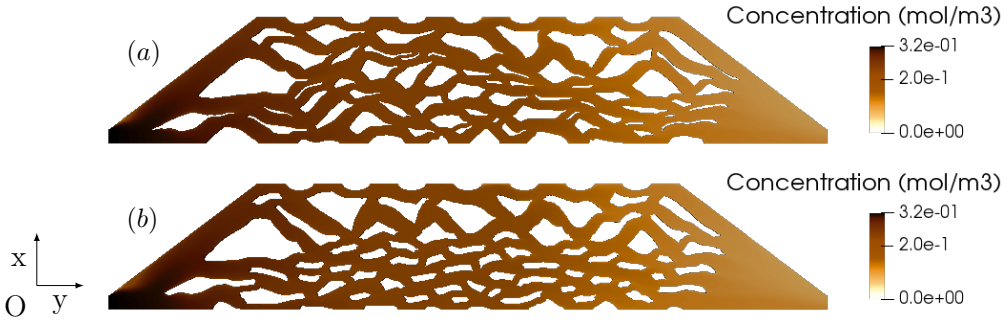

Figure 10: Optimized shape without manufacturing constraints (a), optimized shape with manufacturing constraints (b).

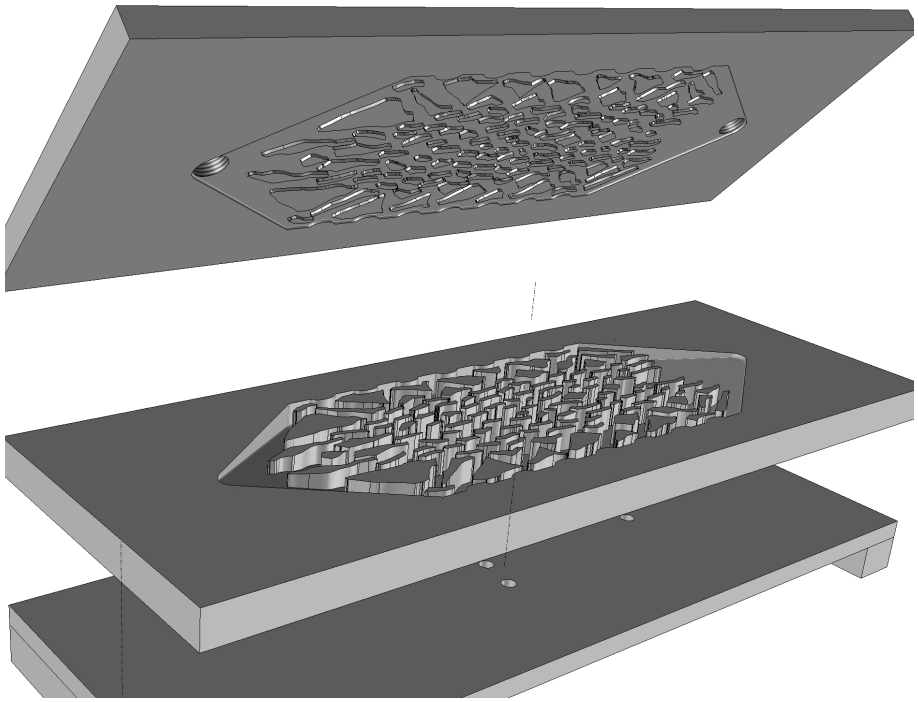

Figure 11: Virtual image of the optimal reactor (Fig 10(c)) manufactured by stratoconception.

energy dissipation and the manufacturing constraints, was determined. However, the optimization algorithm developed exhibits some limitations which should be further investigated. Among these limitations, the treatment of the manufacturing constraints which is not robust. It suffers from too much rigidity since it does not allow constraints to be violated during the optimization process. Another limitation concerns the computation time which takes more than 2 days to converge (simulations performed on a 3.7GHz Xeon Dell Computer 5810). Parallel computing would not improve computational time because the method developped is an iterative method and the number of cells in the mesh is around 50000-70000. On the other hand, it is worth noticing that the use of

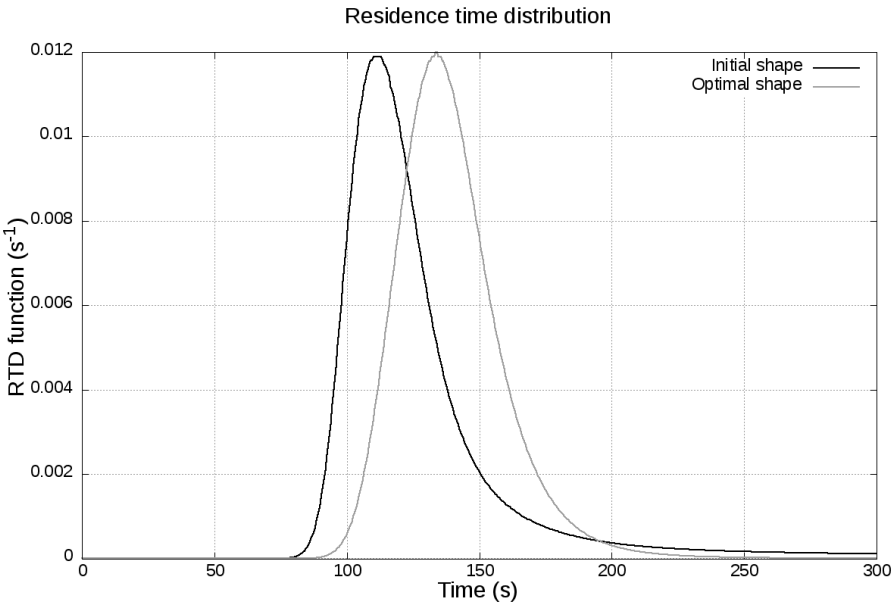

Figure 12: Residence time distribution of initial and optimized shapes.

a geometric algorithm does not allow us to modify the domain topology. Therefore, an interesting issue to be addressed is to allow topology changes within the optimization procedure.

As a close perspective, we are also currently working on generalizing our approach to other types of reactors, which requires to consider 3D geometries.

A Proof of Theorem 2

The well-posed character of System (13)-(14) is standard. Regarding (13), the proof is exactly similar to the one for System (3). We thus refer to [Boy05, FAB+19]. Regarding now System (14), we claim that the proof is a direct adaptation of [HP10, Prop. 1]. This point being clarified, it remains to express $J'(\Omega)(\boldsymbol{\theta})$ under the form $\int_{\partial\Omega} G(\boldsymbol{\theta}\cdot\boldsymbol{n})$, where G denotes the so-called shape gradient of J. We start from the expression (10) of $J'(\Omega)(\boldsymbol{\theta})$.

Let us multiply the first equation of (14) by $\boldsymbol{U'}$ and then integrate by parts. We get

$$-\nu\int_\Omega \Delta \boldsymbol{U}_a\cdot\boldsymbol{U'}\,dx+\int_\Omega(\nabla\boldsymbol{U})^\top\boldsymbol{U_a}\cdot\boldsymbol{U'}\,dx-\int_\Omega\nabla\boldsymbol{U_a}\boldsymbol{U}\cdot\boldsymbol{U'}\,dx$$
$$+\int_\Omega\nabla p_a\cdot\boldsymbol{U'}\,dx=-\int_\Omega C_a\nabla C\cdot\boldsymbol{U'}\,dx.$$

Integrating each term by parts yields successively

$$\begin{aligned}
-\nu\int_\Omega \Delta \boldsymbol{U}_a\cdot\boldsymbol{U'}\,dx &\underset{(11c)}{=} 2\nu\int_\Omega \varepsilon(\boldsymbol{U_a}):\varepsilon(\boldsymbol{U'})\,dx - 2\nu\int_{\Gamma_{out}\cup\Gamma}\varepsilon(\boldsymbol{U_a})\boldsymbol{n}\cdot\boldsymbol{U'}\,d\sigma\\
\int_\Omega (\nabla\boldsymbol{U})^\top\boldsymbol{U_a}\cdot\boldsymbol{U'}\,dx &\underset{(1d)\text{ and }(11c)}{=} -\int_\Omega(\nabla\boldsymbol{U_a})\boldsymbol{U'}\cdot\boldsymbol{U}\,dx+\int_{\Gamma_{out}}(\boldsymbol{U}\cdot\boldsymbol{U_a})(\boldsymbol{U'}\cdot\boldsymbol{n})\,d\sigma\\
-\int_\Omega(\nabla\boldsymbol{U_a})\boldsymbol{U}\cdot\boldsymbol{U'}\,dx &\underset{(1d)\text{ and }(11c)}{=} \int_\Omega(\nabla\boldsymbol{U'})\boldsymbol{U}\cdot\boldsymbol{U_a}\,dx-\int_{\Gamma_{out}}(\boldsymbol{U}\cdot\boldsymbol{n})(\boldsymbol{U'}\cdot\boldsymbol{U_a})\,d\sigma\\
\int_\Omega\nabla p_a\cdot\boldsymbol{U'}\,dx &\underset{(11b)\text{ and }(11c)}{=} \int_{\Gamma_{out}\cup\Gamma}p_a(\boldsymbol{U'}\cdot\boldsymbol{n})\,d\sigma.
\end{aligned}$$

It follows that

$$\begin{aligned}
\int_\Omega\big(2\nu\varepsilon(\boldsymbol{U_a}):\varepsilon(\boldsymbol{U'})-(\nabla\boldsymbol{U_a})\boldsymbol{U'}\cdot\boldsymbol{U}+(\nabla\boldsymbol{U'})\boldsymbol{U}\cdot\boldsymbol{U_a}\big)\,dx&\\
-\int_{\Gamma_{out}}\big((\boldsymbol{U}\cdot\boldsymbol{U_a})(\boldsymbol{U'}\cdot\boldsymbol{n})-(\boldsymbol{U}\cdot\boldsymbol{n})(\boldsymbol{U'}\cdot\boldsymbol{U_a})\sigma(\boldsymbol{U_a},p_a)\boldsymbol{n}\cdot\boldsymbol{U'}\big)\,d\sigma&\\
-\int_\Gamma\sigma(\boldsymbol{U_a},p_a)\boldsymbol{n}\cdot\boldsymbol{U'}\,d\sigma=-\int_\Omega C_a\nabla C\cdot\boldsymbol{U'}\,dx.&\quad(22)
\end{aligned}$$

Let us multiply the first equation of (11) by $\boldsymbol{U_a}$ and then integrate by parts on Ω. One gets

$$-\nu\int_\Omega\Delta\boldsymbol{U'}\cdot\boldsymbol{U_a}\,dx+\int_\Omega(\nabla\boldsymbol{U})\boldsymbol{U'}\cdot\boldsymbol{U_a}\,dx+\int_\Omega(\nabla\boldsymbol{U'})\boldsymbol{U}\cdot\boldsymbol{U_a}\,dx+\int_\Omega\nabla p'\cdot\boldsymbol{U_a}\,dx=0\qquad(23)$$

Integrating each term by parts yields successively

$$\begin{aligned}
-\nu\int_\Omega\Delta\boldsymbol{U'}\cdot\boldsymbol{U_a}\,dx &\underset{(14c)}{=} 2\nu\int_\Omega\varepsilon(\boldsymbol{U_a}):\varepsilon(\boldsymbol{U'})\,dx-2\nu\int_{\Gamma_{out}}\varepsilon(\boldsymbol{U'})\boldsymbol{n}\cdot\boldsymbol{U_a}\,d\sigma\\
\int_\Omega(\nabla\boldsymbol{U})\boldsymbol{U'}\cdot\boldsymbol{U_a}\,dx &\underset{(1d)\text{ and }(11c)}{=} -\int_\Omega(\nabla\boldsymbol{U_a})\boldsymbol{U'}\cdot\boldsymbol{U}\,dx+\int_{\Gamma_{out}}(\boldsymbol{U}\cdot\boldsymbol{U'})(\boldsymbol{U_a}\cdot\boldsymbol{n})\,d\sigma\\
\int_\Omega\nabla p'\cdot\boldsymbol{U_a}\,dx &\underset{(14b)\text{ and }(14c)}{=}\int_{\Gamma_{out}} p'(\boldsymbol{U_a}\cdot\boldsymbol{n})\,d\sigma
\end{aligned}$$

By taking into account the computations above and the boundary conditions (11e) on $\boldsymbol{U'}$, we rewrite(23) as

$$\begin{aligned}
\int_\Omega\big(2\nu\varepsilon(\boldsymbol{U_a}):\varepsilon(\boldsymbol{U'})-(\nabla\boldsymbol{U_a})\boldsymbol{U'}\cdot\boldsymbol{U}+(\nabla\boldsymbol{U'})\boldsymbol{U}\cdot\boldsymbol{U_a}\big)\,dx&\\
+\int_{\Gamma_{out}}(\boldsymbol{U}\cdot\boldsymbol{U_a})(\boldsymbol{U'}\cdot\boldsymbol{n})\,d\sigma=0&\quad(24)
\end{aligned}$$

Combining (22) and (24) yields

$$\int_\Omega C_a\nabla C\cdot\boldsymbol{U'}\,dx=\int_{\Gamma\cup\Gamma_{out}}\sigma(\boldsymbol{U_a},p_a)\boldsymbol{n}\cdot\boldsymbol{U'}\,d\sigma\int_{\Gamma_{out}}(\boldsymbol{U}\cdot\boldsymbol{n})(\boldsymbol{U'}\cdot\boldsymbol{U_a})\,d\sigma\qquad(25)$$

Let us now use the same approach to deal with (12) and (13). We multiply the first equation of (13) by C' and then integrate by parts. We get

$$-D\int_\Omega\Delta C_aC'\,dx-\int_\Omega(\boldsymbol{U}\cdot\nabla C_a)C'\,dx+k\int_\Omega C_aC'\,dx=0\qquad(26)$$

Integrating each term by parts yields

$$\begin{aligned} -D\int_\Omega \Delta C_a C'\,dx &= D\int_\Omega (\nabla C_a\cdot\nabla C')\,dx - D\int_{\partial\Omega}\frac{\partial C_a}{\partial n}C'\,d\sigma \\ \int_\Omega (\boldsymbol{U}\cdot\nabla C_a)C'\,dx &= -\int_\Omega (\boldsymbol{U}\cdot\nabla C')C_a\,dx + \int_{\partial\Omega}(\boldsymbol{U}\cdot\boldsymbol{n})(C_aC')\,d\sigma \end{aligned}$$

Thus, (26) rewrites

$$D\int_\Omega (\nabla C_a\cdot\nabla C')\,dx - D\int_{\partial\Omega}\frac{\partial C_a}{\partial n}C'\,d\sigma + \int_\Omega (\boldsymbol{U}\cdot\nabla C')C_a\,dx - \int_{\partial\Omega}(\boldsymbol{U}\cdot\boldsymbol{n})(C_aC')\,d\sigma + k\int_\Omega C_aC'\,dx = 0 \quad (27)$$

Similarly, let us multiply the first equation of (12) by C_a and then integrate by parts. We obtain

$$-D\int_\Omega \Delta C' C_a\,dx + \int_\Omega (\boldsymbol{U}\cdot\nabla C')C_a\,dx + \int_\Omega (\boldsymbol{U'}\cdot\nabla C)C_a\,dx + k\int_\Omega C_aC'\,dx = 0 \quad (28)$$

which also rewrites

$$D\int_\Omega (\nabla C_a\cdot\nabla C')\,dx - D\int_{\partial\Omega}\frac{\partial C'}{\partial n}C_a\,d\sigma + \int_\Omega (\boldsymbol{U}\cdot\nabla C')C_a\,dx + \int_\Omega (\boldsymbol{U'}\cdot\nabla C)C_a\,dx + k\int_\Omega C_aC'\,dx = 0 \quad (29)$$

Combining (27) and (29) leads to

$$\int_\Omega (\boldsymbol{U'}\cdot\nabla C)C_a\,dx + \underbrace{\int_{\partial\Omega}(\boldsymbol{U}\cdot\boldsymbol{n})(C_aC')\,d\sigma + D\int_{\partial\Omega}\frac{\partial C_a}{\partial n}C'\,d\sigma - D\int_{\partial\Omega}\frac{\partial C'}{\partial n}C_a\,d\sigma}_{\boxed{\mathrm{I}}} = 0. \quad (30)$$

Observe that $\boxed{\mathrm{I}}$ has no contribution on Γ_{in} and Γ_{lat}. Furthermore, one has

$$\begin{aligned} \boxed{\mathrm{I}} - \int_{\Gamma_{out}} C'\,d\sigma &= -D\int_\Gamma C_a\left(-\frac{\partial C^2}{\partial n^2}(\boldsymbol{\theta}\cdot\boldsymbol{n}) + \nabla C\cdot(\nabla(\boldsymbol{\theta}\cdot\boldsymbol{n}) - (\nabla(\boldsymbol{\theta}\cdot\boldsymbol{n})\cdot\boldsymbol{n})\boldsymbol{n})\right)d\sigma \\ &= -D\int_\Gamma C_a\left(-\frac{\partial C^2}{\partial n^2}(\boldsymbol{\theta}\cdot\boldsymbol{n}) + \nabla C\cdot\nabla(\boldsymbol{\theta}\cdot\boldsymbol{n}) - \nabla C\cdot(\nabla(\boldsymbol{\theta}\cdot\boldsymbol{n})\cdot\boldsymbol{n})\boldsymbol{n}\right)d\sigma \\ &= -D\int_\Gamma C_a\left(-\frac{\partial C^2}{\partial n^2}(\boldsymbol{\theta}\cdot\boldsymbol{n}) + \nabla C\cdot\nabla(\boldsymbol{\theta}\cdot\boldsymbol{n}) - (\nabla(\boldsymbol{\theta}\cdot\boldsymbol{n})\cdot\boldsymbol{n})(\nabla C\cdot\boldsymbol{n})\right)d\sigma \\ &= -D\int_\Gamma C_a\left(-\frac{\partial C^2}{\partial n^2}(\boldsymbol{\theta}\cdot\boldsymbol{n}) + \nabla C\cdot\nabla(\boldsymbol{\theta}\cdot\boldsymbol{n}) - \frac{\partial(\boldsymbol{\theta}\cdot\boldsymbol{n})}{\partial n}\frac{\partial C}{\partial n}\right)d\sigma \end{aligned}$$

according to (12). Since Γ is the only part of the boundary of Ω met by the support of $\boldsymbol{\theta}$, it is

legitimate to use an integration by parts formula[2] on $\partial\Omega$. It yields

$$\boxed{\mathrm{I}} - \int_{\Gamma_{out}} C'\, d\sigma = D\int_\Gamma C_a\left(\Delta C(\boldsymbol{\theta}\cdot\boldsymbol{n}) - \mathcal{H}\frac{\partial C}{\partial n}(\boldsymbol{\theta}\cdot\boldsymbol{n})\right) \underset{(3c)}{=} D\int_\Gamma C_a\Delta C(\boldsymbol{\theta}\cdot\boldsymbol{n}) \tag{32}$$

Hence, (30) reads

$$\int_\Omega (\boldsymbol{U'}\cdot\nabla C)C_a\, dx + J'(\Omega)(\boldsymbol{\theta}) + \mathcal{D}\int_\Gamma C_a\Delta C(\boldsymbol{\theta}\cdot\boldsymbol{n}) = 0 \tag{33}$$

By combining (25) and (33), we obtain

$$\begin{aligned} J'(\Omega)(\boldsymbol{\theta}) \quad &= \quad -\int_{\Gamma\cup\Gamma_{out}} \sigma(\boldsymbol{U_a}, p_a).n\cdot\boldsymbol{U'}\, d\sigma - D\int_\Gamma C_a\Delta C(\boldsymbol{\theta}\cdot\boldsymbol{n}) \\ &\quad -\int_{\Gamma_{out}} (\boldsymbol{U}\cdot\boldsymbol{n})(\boldsymbol{U'}\cdot\boldsymbol{U_a})\, d\sigma. \end{aligned} \tag{34}$$

Finally, using the boundary conditions (11c), (11d) and (44d) leads to

$$J'(\Omega)(\boldsymbol{\theta}) = \int_\Gamma \left((2\nu\varepsilon(\boldsymbol{U_a})\boldsymbol{n} - p_a\boldsymbol{n})\cdot\frac{\partial\boldsymbol{U}}{\partial n} - DC_a\Delta C\right)(\boldsymbol{\theta}\cdot\boldsymbol{n})\, d\sigma \tag{35}$$

To conclude, it remains to rewrite the expression above in a more symmetrical way. To this aim, we will use the following lemma whose proof is postponed at the en d of this section for the sake of clarity.

Lemma 1. *Assume that $\partial\Omega$ is smooth enough so that $\boldsymbol{U}$ and $\boldsymbol{U_a}$ belong to $H^2(\Omega)$. Thus, one has on Γ*

$$\boldsymbol{n}\cdot\frac{\partial\boldsymbol{U}}{\partial n} = 0 \tag{36}$$

$$\varepsilon(\boldsymbol{U})\boldsymbol{n}\cdot\frac{\partial\boldsymbol{U}}{\partial n} = |\varepsilon(\boldsymbol{U})|^2 \tag{37}$$

$$(\varepsilon(\boldsymbol{U_a})\boldsymbol{n})\cdot\frac{\partial\boldsymbol{U}}{\partial n} = \varepsilon(\boldsymbol{U}):\varepsilon(\boldsymbol{U_a}) \tag{38}$$

Roughly speaking, this follows from the fact that ($\boldsymbol{U}$ and $\boldsymbol{U_a}$) are divergence-free in Ω and vanish on Γ. Finally, this leads to the desired expression of the shape derivative:

$$J'(\Omega)(\boldsymbol{\theta}) = \int_\Omega \left(2\nu(\varepsilon(\boldsymbol{U}):\varepsilon(\boldsymbol{U_a}) - DC_a\Delta C\right)(\boldsymbol{\theta}\cdot\boldsymbol{n})\, d\sigma \tag{39}$$

Proof of Lemma 1. Let us first show (36). Since $\boldsymbol{U}$ vanishes on Γ, one has $\nabla\boldsymbol{U} = (\nabla\boldsymbol{U}\boldsymbol{n})\boldsymbol{n}$. It follows that $\partial U_i/\partial x_i = n_i\partial U_i/\partial n$ and therefore

$$\boldsymbol{n}\cdot\frac{\partial\boldsymbol{U}}{\partial n} = \sum_i n_i\frac{\partial U_i}{\partial n} = \sum_i \frac{\partial U_i}{\partial x_i} = \mathrm{div}(\boldsymbol{U}) = 0 \quad \text{on } \Gamma.$$

[2] Recall that if $f\in H^2(\Omega)$ and $g\in H^3(\Omega)$, then one has

$$\int_{\partial\Omega}\nabla f\cdot\nabla g\, d\sigma = -\int_{\partial\Omega} f\Delta g\, d\sigma + \int_{\partial\Omega}\left(\frac{\partial f}{\partial n}\frac{\partial g}{\partial n} + f\frac{\partial^2 g}{\partial n^2} + \mathcal{H}f\frac{\partial g}{\partial n}\right) d\sigma \tag{31}$$

where $\mathcal{H}$ denotes the mean curvature on $\partial\Omega$ (see [HP18, Chapter 5]).

Let us now prove (38). Using the same tricks as above enable us to write

$$\frac{\partial U_i}{\partial x_j} = \frac{\partial U_i}{\partial n} n_j \quad \text{and} \quad \operatorname{div} \boldsymbol{U} = \sum_i \frac{\partial U_i}{\partial x_i} = \sum_i \frac{\partial U_i}{\partial n} n_i = 0$$

from which we infer that

$$\begin{aligned} \varepsilon(\boldsymbol{U})\boldsymbol{n} &= \frac{1}{2}\left(\sum_j \left(\frac{\partial U_i}{\partial x_j} + \frac{\partial U_j}{\partial x_i}\right) n_j\right)_i = \frac{1}{2}\left(\sum_j \frac{\partial U_i}{\partial n} n_j^2 + \frac{\partial U_j}{\partial n} n_i n_j\right)_i \\ &= \frac{1}{2}\left(\frac{\partial U_i}{\partial n}\sum_j n_j^2\right)_i = \frac{1}{2}\left(\frac{\partial U_i}{\partial n}\right)_i = \frac{1}{2}\frac{\partial \boldsymbol{U}}{\partial \boldsymbol{n}} \end{aligned}$$

on Γ. It follows that $(\varepsilon(\boldsymbol{U_a})\boldsymbol{n}) \cdot \frac{\partial \boldsymbol{U}}{\partial n} = 2(\varepsilon(\boldsymbol{U_a})\boldsymbol{n}) \cdot (\varepsilon(\boldsymbol{U})\boldsymbol{n})$ on Γ and then

$$\begin{aligned} (\varepsilon(\boldsymbol{U_a})\boldsymbol{n}) \cdot \frac{\partial \boldsymbol{U}}{\partial n} &= \frac{1}{2}\sum_i \sum_j \left(\frac{\partial U_{a_i}}{x_j} + \frac{\partial U_{a_j}}{x_i}\right) n_j \sum_l \left(\frac{\partial U_i}{x_l} + \frac{\partial U_l}{x_i}\right) n_l \\ &= \frac{1}{2}\sum_{i,j,l} \left(\frac{\partial U_{a_i}}{\partial \boldsymbol{n}} n_j^2 + \frac{\partial U_{a_j}}{\partial \boldsymbol{n}} n_i n_j\right)\left(\frac{\partial U_i}{\partial \boldsymbol{n}} n_l^2 + \frac{\partial U_l}{\partial \boldsymbol{n}} n_i n_l\right) \\ &= \frac{1}{2}\sum_{i,j,l} \left(\frac{\partial U_{a_i}}{\partial \boldsymbol{n}}\frac{\partial U_i}{\partial \boldsymbol{n}} n_j^2 n_l^2 + \underbrace{\frac{\partial U_{a_j}}{\partial \boldsymbol{n}} n_j}_{\operatorname{div} \boldsymbol{U_a}=0} \underbrace{\frac{\partial U_i}{\partial \boldsymbol{n}} n_i}_{\operatorname{div} \boldsymbol{U}=0} n_l^2 + \frac{\partial U_{a_i}}{\partial \boldsymbol{n}} n_i \frac{\partial U_l}{\partial \boldsymbol{n}} n_l n_j^2 + \frac{\partial U_{a_j}}{\partial \boldsymbol{n}} n_j \frac{\partial U_l}{\partial \boldsymbol{n}} n_l n_i^2\right). \end{aligned}$$

The three last terms of the sum vanish (since $\operatorname{div} \boldsymbol{U} = \operatorname{div} \boldsymbol{U_a} = 0$ on Γ) and then,

$$2(\varepsilon(\boldsymbol{U_a})\boldsymbol{n}) \cdot (\varepsilon(\boldsymbol{U})\boldsymbol{n}) = \frac{1}{2}\sum_i \frac{\partial U_{a_i}}{\partial \boldsymbol{n}}\frac{\partial U_i}{\partial \boldsymbol{n}} \tag{40}$$

On the other hand, one has

$$\begin{aligned} \varepsilon(\boldsymbol{U}) : \varepsilon(\boldsymbol{U_a}) &= \frac{1}{4}\sum_{i,j} \left(\frac{\partial U_i}{\partial x_j} + \frac{\partial U_j}{\partial x_i}\right)\left(\frac{\partial U_{a_i}}{\partial x_j} + \frac{\partial U_{a_j}}{\partial x_i}\right) \\ &= \frac{1}{4}\sum_{i,j} \left(\frac{\partial U_i}{\partial x_j}\frac{\partial U_{a_i}}{\partial x_j} + \frac{\partial U_j}{\partial x_i}\frac{\partial U_{a_i}}{\partial x_j} + \frac{\partial U_i}{\partial x_j}\frac{\partial U_{a_j}}{\partial x_i} + \frac{\partial U_j}{\partial x_i}\frac{\partial U_{a_j}}{\partial x_i}\right) \\ &= \frac{1}{2}\sum_{i,j} \left(\frac{\partial U_i}{\partial x_j}\frac{\partial U_{a_i}}{\partial x_j} + \frac{\partial U_j}{\partial x_i}\frac{\partial U_{a_i}}{\partial x_j}\right) = \frac{1}{2}\sum_{i,j} \left(\frac{\partial U_i}{\partial \boldsymbol{n}}\frac{\partial U_{a_i}}{\partial \boldsymbol{n}} n_j^2 + \frac{\partial U_j}{\partial \boldsymbol{n}}\frac{\partial U_{a_i}}{\partial \boldsymbol{n}} n_i n_j\right) \\ &= \frac{1}{2}\sum_i \frac{\partial U_i}{\partial \boldsymbol{n}}\frac{\partial U_{a_i}}{\partial \boldsymbol{n}} \underbrace{\sum_j n_j^2}_{=1} + \frac{1}{2}\underbrace{\sum_j \frac{\partial U_j}{\partial \boldsymbol{n}} n_j}_{\operatorname{div} \boldsymbol{U}=0} + \frac{1}{2}\underbrace{\sum_i \frac{\partial U_{a_i}}{\partial \boldsymbol{n}} n_i}_{\operatorname{div} \boldsymbol{U_a}=0} = \frac{1}{2}\sum_i \frac{\partial U_i}{\partial \boldsymbol{n}}\frac{\partial U_{a_i}}{\partial \boldsymbol{n}}, \end{aligned}$$

whence (38). The proof of (37) is exactly similar. □

B Proof of Proposition 1

Let us first recall (see for instance [All07, HP18, DFOP18]) that

$$C_1'(\Omega)(\boldsymbol{\theta}) = \frac{d}{dt}\left(\int_{\Omega_t} 1\, dx \Big|_{t=0} - \mathcal{V}(\Omega_0) \right) = \int_{\partial\Omega} (\boldsymbol{\theta}\cdot\boldsymbol{n}) d\sigma \tag{41}$$

$$\begin{aligned} C_2'(\Omega)(\boldsymbol{\theta}) &= \frac{d}{dt}\left(2\nu \int_{\Omega_t} |\varepsilon(\boldsymbol{U})|^2\, dx \Big|_{t=0} - \mathcal{E}(\Omega_0) \right) &(42)\\ &= 2\nu \int_{\partial\Omega} |\varepsilon(\boldsymbol{U})|^2 (\boldsymbol{\theta}\cdot\boldsymbol{n})\, d\sigma + 4\nu \int_{\Omega} \varepsilon(\boldsymbol{U}) : \varepsilon(\boldsymbol{U'})\, dx &(43)\end{aligned}$$

It is standard to rewrite $C_2'(\Omega)(\boldsymbol{\theta})$ in a more workable form, by introducing a well-chosen adjoint method. In accordance with [DFOP18], let us introduce the adjoint state $(\boldsymbol{U_a}, p_a)$ solving the linearized Navier-Stokes system

$$\begin{aligned} -\nu\Delta \boldsymbol{U_a} + (\nabla \boldsymbol{U})^\top \boldsymbol{U_a} - \nabla \boldsymbol{U_a} \boldsymbol{U} + \nabla p_a &= -\lambda_{\mathcal{E}} 2\nu \Delta \boldsymbol{U} \quad \text{in } \Omega &(44a)\\ \nabla \cdot \boldsymbol{U_a} &= 0 \quad \text{in } \Omega &(44b)\\ \boldsymbol{U_a} &= 0 \quad \text{on } \Gamma_{in} \cup \Gamma_{lat} \cup \Gamma &(44c)\\ \sigma(\boldsymbol{U_a}, p_a)\boldsymbol{n} + (\boldsymbol{U}\cdot\boldsymbol{n})\boldsymbol{U_a} &= 4\nu\lambda_{\mathcal{E}} \varepsilon(\boldsymbol{U})\boldsymbol{n} \quad \text{on } \Gamma_{out} &(44d)\end{aligned}$$

Hence, one shows with the help of well-adapted integrations by parts that the quantity $C_2'(\Omega)(\boldsymbol{\theta})$ rewrites

$$C_2'(\Omega)(\boldsymbol{\theta}) = \int_{\Omega} \left(2\nu(\varepsilon(\boldsymbol{U}) : \varepsilon(\boldsymbol{U_a}) - \lambda_{\mathcal{E}} \varepsilon(\boldsymbol{U}) : \varepsilon(\boldsymbol{U}))\right) (\boldsymbol{\theta}\cdot\boldsymbol{n})\, d\sigma$$

The expected conclusion hence follows by combining these formula with the result of Proposition 2.

References

[ADE+17a] G. Allaire, C. Dapogny, R. Estevez, A. Faure, and G. Michailidis, Structural optimization under overhang constraints imposed by additive manufacturing technologies, J. Comput. Phys. **351** (2017), 295–328. MR 3713427

[ADE+17b] Grégoire Allaire, Charles Dapogny, Rafael Estevez, Alexis Faure, and Georgios Michailidis, Structural optimization under overhang constraints imposed by additive manufacturing processes: an overview of some recent results, Appl. Math. Nonlinear Sci. **2** (2017), no. 2, 385–402. MR 3896926

[ADFM17] Grégoire Allaire, Charles Dapogny, Alexis Faure, and Georgios Michailidis, Shape optimization of a layer by layer mechanical constraint for additive manufacturing, C. R. Math. Acad. Sci. Paris **355** (2017), no. 6, 699–717. MR 3661554

[AJM16] G. Allaire, F. Jouve, and G. Michailidis, Thickness control in structural optimization via a level set method, Struct. Multidiscip. Optim. **53** (2016), no. 6, 1349–1382. MR 3498891

[All07] G. Allaire, Conception optimale de structures, Collection Mathématiques et Applications, vol. 58, Springer, 2007.

[Att95] Dominique Attali, Squelettes et graphes de voronoi 2d et 3d, Ph.D. thesis, 1995.

[BF13] Franck Boyer and Pierre Fabrie, Mathematical tools for the study of the incompressible Navier-Stokes equations and related models, Applied Mathematical Sciences, vol. 183, Springer, New York, 2013. MR 2986590

[BOP18] Matthieu Bonnivard, Florian Omnès, and Yannick Privat, Modeling and optimization of hourglass-shaped aquaporins, Math. Models Methods Appl. Sci. **28** (2018), no. 8, 1529–1564. MR 3827964

[Boy05] Franck Boyer, Trace theorems and spatial continuity properties for the solutions of the transport equation, Differential Integral Equations **18** (2005), no. 8, 891–934. MR 2150445

[BP13] Maitine Bergounioux and Yannick Privat, Shape optimization with Stokes constraints over the set of axisymmetric domains, SIAM J. Control Optim. **51** (2013), no. 1, 599–628. MR 3032888

[DFOP18] Charles Dapogny, Pascal Frey, Florian Omnès, and Yannick Privat, Geometrical shape optimization in fluid mechanics using FreeFem++, Struct. Multidiscip. Optim. **58** (2018), no. 6, 2761–2788. MR 3878725

[dLSMP11] Xavier Dubois de La Sablonière, Benjamin Mauroy, and Yannick Privat, Shape minimization of the dissipated energy in dyadic trees, Discrete Contin. Dyn. Syst. Ser. B **16** (2011), no. 3, 767–799. MR 2806322

[DMNV07] G. Dogan, P. Morin, R. H. Nochetto, and M. Verani, Discrete gradient flows for shape optimization and applications, Computer Methods in Applied Mechanics and Engineering **196** (2007), no. 37, 3898–3914.

[FAB+19] F. Feppon, G. Allaire, F. Bordeu, J. Cortial, and C. Dapogny, Shape optimization of a coupled thermal fluid-structure problem in a level set mesh evolution framework, SeMA J. **76** (2019), no. 3, 413–458. MR 3990998

[Fed59] Herbert Federer, Curvature measures, Trans. Amer. Math. Soc. **93** (1959), 418–491. MR 110078

[Hol15] Gerhard Holzinger, Openfoam: A little user-manual, CD-Laboratory-Particulate Flow Modelling, Johannes Keplper University: Linz, Austria (2015).

[HP10] Antoine Henrot and Yannick Privat, What is the optimal shape of a pipe?, Arch. Ration. Mech. Anal. **196** (2010), no. 1, 281–302. MR 2601075

[HP18] A. Henrot and M. Pierre, Shape variation and optimization: a geometrical analysis, Tracts in Mathematics, vol. 28, European Mathematical Society, Zurich, 2018.

[MP10] B. Mohammadi and O. Pironneau, Applied shape optimization for fluids, Oxford University Press, 2010.

[MS76] F Murat and J Simon, Sur le contrôle par un domaine géométrique, Pré-publication du Laboratoire d'Analyse Numérique,(76015) (1976).

[SZ92] J. Sokolowski and J.-P. Zolésio, Introduction to shape optimization: shape sensitivity analysis, Springer, 1992.

[Tem84] Roger Temam, Navier-Stokes equations, third ed., Studies in Mathematics and its Applications, vol. 2, North-Holland Publishing Co., Amsterdam, 1984, Theory and numerical analysis, With an appendix by F. Thomasset. MR 769654

[TKH10] Osamu Tonomura, Manabu Kano, and Shinji Hasebe, Shape optimization of microchannels using cfd and adjoint method, 20th European Symposium on Computer Aided Process Engineering (S. Pierucci and G. Buzzi Ferraris, eds.), Computer Aided Chemical Engineering, vol. 28, Elsevier, 2010, pp. 37 – 42.

[WTJF98] Henry G Weller, Gavin Tabor, Hrvoje Jasak, and Christer Fureby, A tensorial approach to computational continuum mechanics using object-oriented techniques, Computers in physics **12** (1998), no. 6, 620–631.